The sensitivity of failure analysis of boiler tubes to the shape of elliptical external erosion flaws

Ifeanyi Emmanuel Kalu [a], Helen Mary Inglis [a], Schalk Kok [a]

[a] Centre for Asset Integrity Management, Department of Mechanical and Aeronautical Engineering, University of Pretoria, Pretoria, South Africa.

Highlights

- Geometric functions to enable the accurate modelling of boiler tubes with localized erosion flaws were developed.
- Effect of the flaw geometries on the stress concentrations and failure pressures of the tubes were investigated.
- Failure of the tubes is insensitive to the choice of flaw shape, as long as the minimum remaining tube thickness is matched.
- For various failure criteria thresholds, failure assessment of flawed tubes is fairly insensitive to their flaw shapes.

Abstract

Localized erosion is one of the most common failure mechanisms associated with boiler tubes, driven by impaction of the tube surface by fly ash, soot blowing steam, falling slag or other abrasive substances from the boiler's combustion chamber. The tubes may experience significant localized reduction in their wall thickness, becoming susceptible to plastic collapse and bursting. The replacement of failed tubes is one of the leading causes of unplanned and forced boiler outages in process and power plants. In this study, geometric functions to enable the accurate modelling of boiler tubes with localized erosion flaws were developed from conceptualized models and finite element analyses were conducted on the modelled flawed tubes. The effect of geometry on the stress concentration in the tubes and on the failure pressure associated with the tubes was investigated. Linear elastic stress analysis is sensitive to the flaw geometry – for representative problem stresses vary 38% as the flaw shape is varied. However, nonlinear elastic-plastic analysis shows significantly reduced sensitivity to flaw shape. The collapse pressure of the same

representative problem now varies only 2.45% as the flaw shape is varied. This finding was demonstrated for various failure thresholds sourced from the literature, based either on plastic strain or Von Mises equivalent stress, which demonstrates that the failure of the tubes is insensitive to the specific choice of shape parameterization, as long as the minimum remaining wall thickness is matched. The outcome of these investigations gives further insight into the behaviour of tubes with localized external flaws while in service.

Keywords: Localized erosion flaws, boiler tubes, plastic collapse, finite element analysis, stress concentration, plastic strain.

1 Introduction

Complex conditions in which boiler tubes operate while in service, involving high temperature, pressure and erosive-corrosive environments, cause them to experience a wide variety of failures [1–5]. These failures include the formation of cracks, pits or gouges, and the deformation, bulging, thinning, and eventual bursting of the tubes [2–7]. The occurrence of these tube failures has been reported to be one of the major causes of availability loss in boilers [7–10] and it is also a leading cause of unscheduled or forced boiler outages in power plants and manufacturing industries, resulting in loss of production and costly emergency repairs [1–3,10–14]. The cost of electricity power loss as a result of boiler tube failures leading to unplanned outages exceeds billions of dollars annually [3]. To improve the profitability of these industries, more focused attention needs to be given to these failure problems.

The concept of localized erosion or metal-loss in boiler tubes has drawn a lot of attention over the years due to the resulting failures [2–4,7–13]. As a result of the continuous exposure of boiler

tubes to impingement by abrasive substances within their operating environment, they experience significant metal loss due to wall thickness reduction. As this localized metal loss continues for a period, the tubes become susceptible to gross plastic collapse, causing an overall structural instability of the tubes such that they lose equilibrium and are unstable for a small increase in load [15,16]. Fig. 1 shows an example of a failed boiler tube, with final rupture due to plastic deformation after wall thinning.

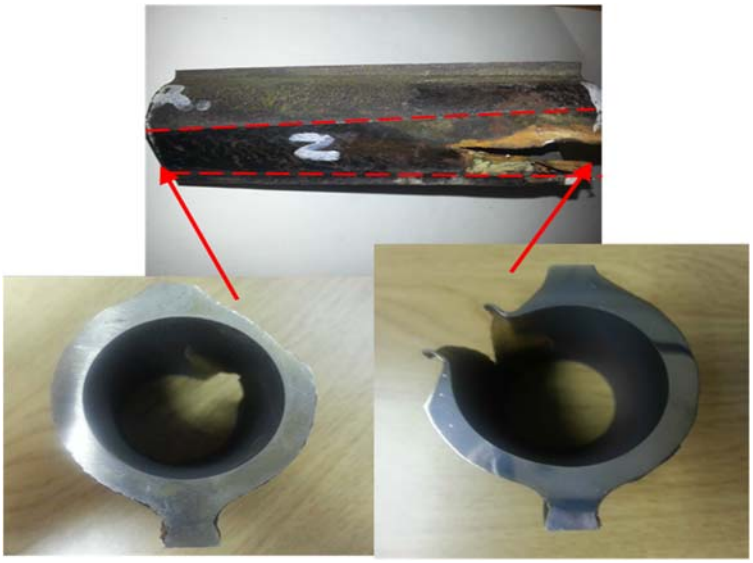

Fig. 1. Side view of a cut-out sample of the failed tube (above) and top view showing the wall thinning of the tube and the ruptured tube (below)

In a typical case of a commercial power plant with ageing infrastructure and a constrained maintenance budget, a quick assessment procedure is required for numerous flawed tubes. The inspection team will have to measure all suspected flawed tubes and prioritize their replacement or repairs, judging whether or not they will remain safe until the next planned outage. The operator captures only limited information for these flawed tubes: typically, the flaw width, flaw length and minimum remaining wall thickness. This limited data only allows a simple parameterization of flaw geometries, but this simple parameterization captures large variations in flaw size. This paper's main focus is to determine how sensitive typical failure assessment procedures are as the

flaw sizes and shapes are varied, while the minimum remaining wall thickness remains unchanged. Such a study gives guidance as to whether more complex descriptions of flaw geometries are necessary, or if simple descriptions are adequate.

Through the years, failure assessment of pressurized vessels under localized erosion (mainly boiler tubes) have been by metallurgical investigations during planned outages [4,17–19] or studying the flaw evolution using some form of fluid-structure interaction [12,20]. Stress- and strain-based criteria have also been proposed by various authors to guard against the failure of pressurized vessels due to local metal loss and consequently plastic collapse. Sims et al [21] proposed a 2% plastic strain ($P_{2\%}$) criteria for round localized thinned flawed vessels, which was also extended to groove-like thinned flawed vessels by Hantz et al. [22]. Shim et al. [23,24], Fekete and Varga [25], and Abdalla Filho et al. [26] used the ultimate tensile strength (σ_{uts}) of the vessel as the referenced failure stress, such that failure is considered when the maximum Von Mises equivalent stress within the vessel reaches σ_{uts}. Y. Kim et al. [27] used 90% σ_{uts} and Choi et al [28]. used the flow strength (which is the average of the yield strength, σ_y and σ_{uts}), 80% and 90% σ_{uts} as failure criteria for their investigative studies. J.W. Kim et al. [29] and Ma et al. [30] recommended using the true ultimate tensile strength $(\sigma_{t,uts})$ as the reference failure stress. Kamaya et al. [31] and Zarrabi [2] proposed using the flow strength as the referenced failure criteria.

In this paper, a wide range of external localized erosion flaws are modelled geometrically, based on flaws observed on boiler tubes in operation. These parameterized geometries are simulated using linear as well as nonlinear finite element analyses (FEA). The effect of varying geometric parameters on the elastic stress concentrations in the tubes is first investigated. Subsequently, the variation in the failure pressure, computed using nonlinear elastic-plastic analysis with a bilinear plasticity model, is characterized. Various failure criteria are used to judge the sensitivity of the

specific failure assessment criterion to the size and shape of the flaw (keeping the minimum remaining wall thickness unchanged). These comparative studies are then used to determine to what extent more complex flaw geometries need to be considered. A broad range of flaws are used for this study, unlike many of the general investigations performed on localized external erosion of boiler tubes, which usually focus on few flaws, sometimes only one or two [11,17–19,32].

2 Geometric functions for modelled localized thinned boiler tubes

Previous finite element analysis (FEA) studies on boiler tubes were done using flaw geometries such as: elliptical scar, triangular scar, rectangular scar, double rectangular scar and part-through rectangular scar [32–34]. These flaw geometries do not resemble the scenarios of localized external erosion which we observed in examples of failed boiler tubes [35]. More similar shapes were used to model erosion of titanium tubes in heat exchangers [18] and corrosion defects on pipes [25]. In this study, three characteristic geometric flaw shapes that will reasonably satisfy a wide range of localized erosion that occur in real scenarios were modelled in the DesignModeler of ANSYS®[36]. Given the data captured in inspection reports (flaw width, flaw length and minimum remaining wall thickness), only one of these models can exactly match the provided flaw data. The design of these models is explained in detail below.

The first modelled localized flaw on the tube is a *u-shaped* or *scoop shaped* flaw, created by offsetting a plane from the centreline of the tube to a height, H, then sketching from the mid-axis of the tube a convex ellipse with an axis offset by a height, z from the tube centre line. This causes the ellipse to intersect with the circular cross section of the tube in a u-shaped manner. The sketch is revolved from the plane axis at H in the horizontal direction to slice-cut the tube to a specific f_d as shown in Fig. 2 and Fig. 3.

The second modelled flaw on the tube is an *n-shaped* or *saddle shaped* flaw. This is created by first offsetting from the tube centreline to a height, H, then sketching a concave ellipse that is offset from the base to a height, z, as well as two vertical straight lines drawn from the plane to the vertices of the ellipse. This causes the ellipse to intersect the circular cross section of the tube in an n-shaped manner. The entire sketch is revolved about the x-axis from the vertical plane and slice-cut to the required flaw depth, f_d on the tube as shown in Fig. 4 and Fig. 5.

The flat line modelled flaw is the third modelled flaw geometry made by offsetting a plane to a height, H, from the centre line of the tube and sketching a horizontal straight line at the specific flaw depth, f_d. The sketch is revolved about the x-axis from the position of the plane to slice and cut the tube to the required flaw depth f_d as shown in Fig. 6 and Fig. 7. The flat line flaw is the point of intersection of the sets of u-shaped and n-shaped flaws, as the major axis of the ellipse becomes infinitely large.

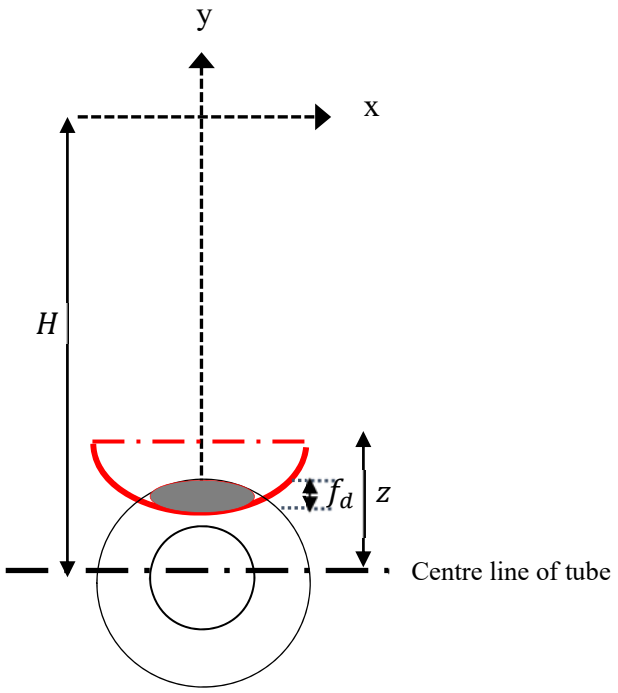

Fig. 2. Schematic showing the modelling of a u-shaped or scoop shaped flawed tube - cross-section.

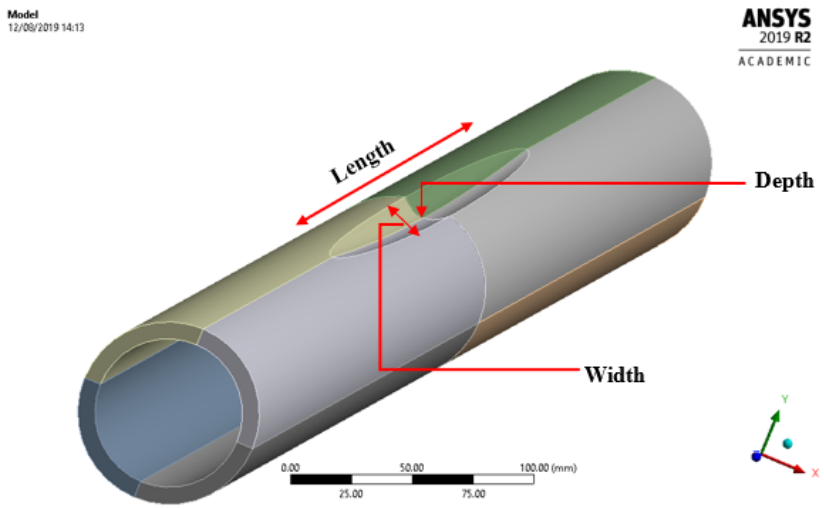

Fig. 3. A u-shaped (scoop shaped) flawed tube.

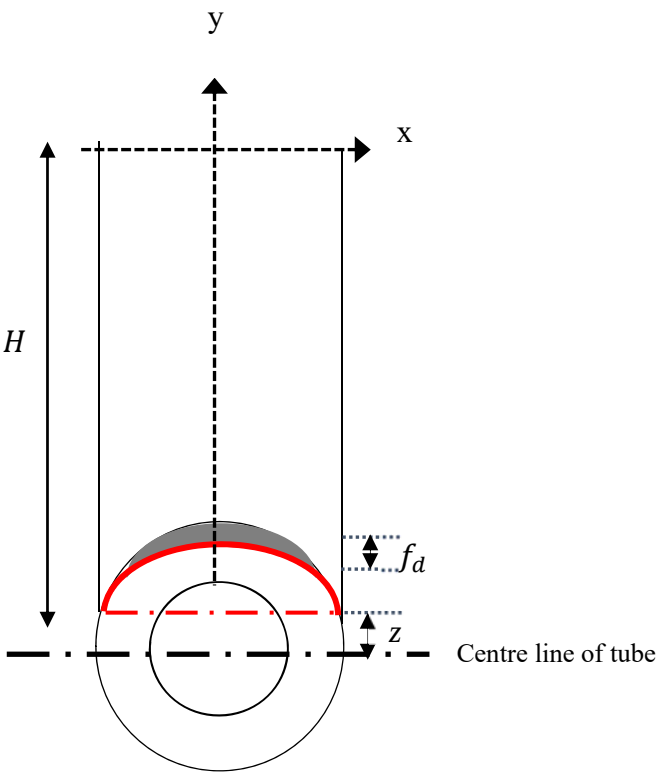

Fig. 4. Schematic showing the modelling of an n-shaped or saddle shaped flawed tube - cross-section.

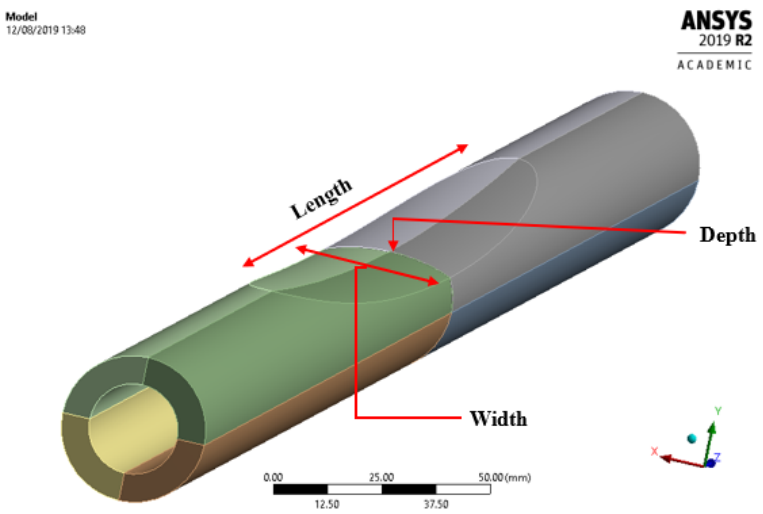

Fig. 5. An n-shaped (saddle shaped) flawed tube.

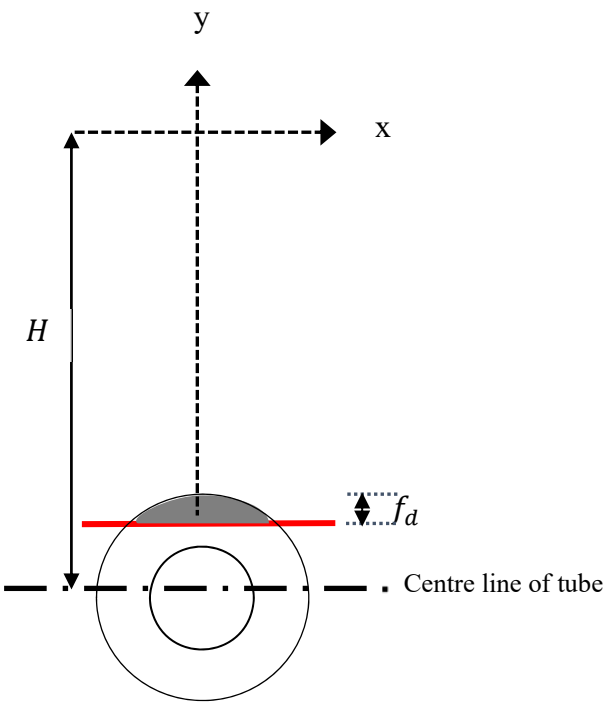

Fig. 6. Schematic showing the modelling of a flat line flawed tube - cross-section.

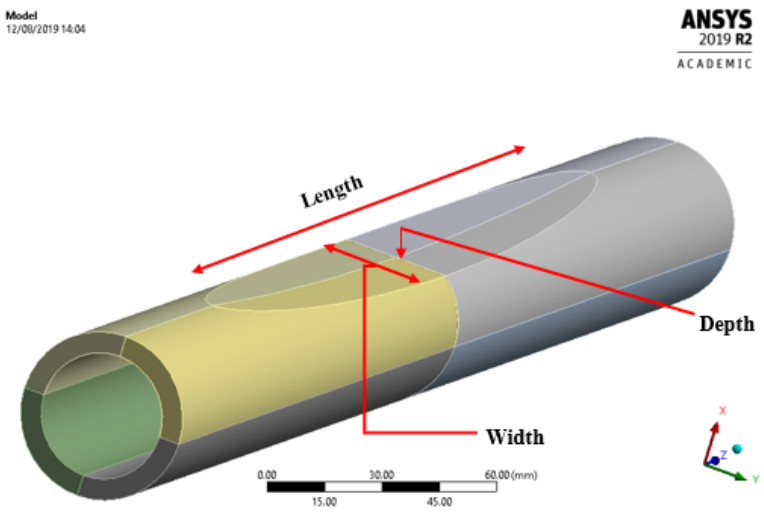

Fig. 7. A flat line flawed tube.

Mathematical expressions for the flaw geometries: the flaw length (f_l), flaw width (f_w), flaw depth (f_d) and remaining thickness on the tube (t_r), are formulated for a tube with an outer diameter (D_o) and tube thickness (t) using the following parameters: Plane height from the centre line of the tube (H), radius of the cutting plane from the plane axis (R), horizontal dimension of the elliptical surface (a), vertical dimension of elliptical surface (b) and remaining thickness of the tube (t_r).

The length of the flaw, f_l , which is the same for all three variants, is derived from the schematic shown in Fig. 8. The cutting radius, R is given by:

$$R = H - [(\frac{D_o}{2}) - f_d] \quad (1)$$

By the Pythagorean theorem,

$$R^2 = (R - f_d)^2 + (\frac{f_l}{2})^2 \quad (2)$$

Rearranging Eq.(2) gives the solution for f_l :

$$f_l = 2\sqrt{2Rf_d - {f_d}^2} \tag{3}$$

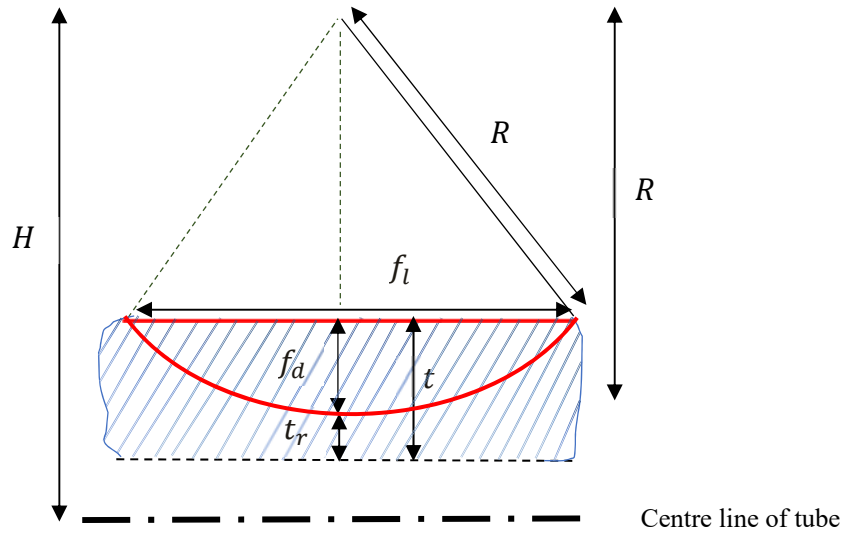

Fig. 8. Schematic showing the creation of the localized flaw length on the tube – side view.

The width f_w of the flat line flaw is derived from Fig. 9, which shows the intersection of the flat line with the circular cross section of the tube. Again, the Pythagorean theorem gives

$$(\tfrac{D_o}{2})^2 = ((\tfrac{D_o}{2}) - f_d)^2 + (\tfrac{f_w}{2})^2 \tag{4}$$

Rearranging Eq. (4) gives the solution for f_w:

$$f_w = 2\sqrt{D_o f_d - {f_d}^2} \tag{5}$$

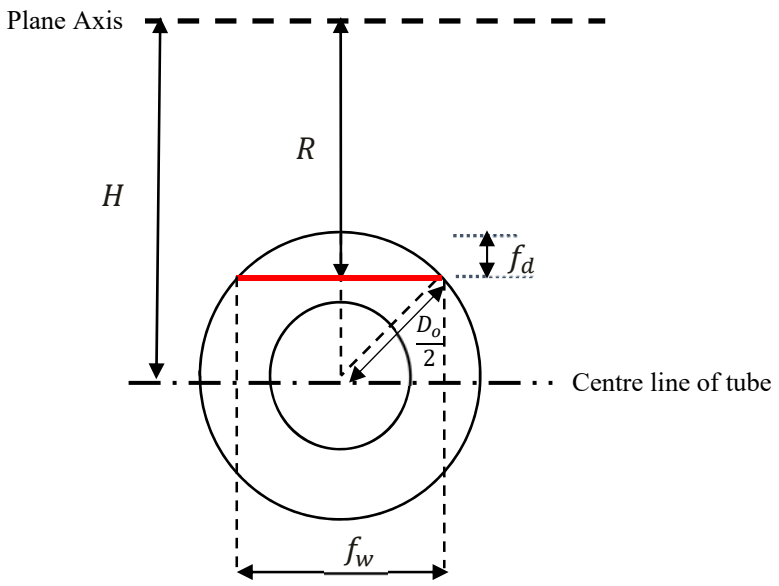

Fig. 9. Front view of the flat line flaw showing the cutting plane in red, intersected with the tube cross-section.

The width f_w of the u-shaped flaw is derived from Fig. 10, which shows the intersection of the convex ellipse with the circular cross section of the tube. The width f_w of the n-shaped flaw is derived from Fig. 11, which shows the intersection of the concave ellipse with the circular cross section of the tube.

From Fig. 10, for the u-shaped flaw:

$$f_d = \frac{D_o}{2} - (H - R) \tag{6}$$

$$f_d = \frac{D_o}{2} - (z + b) \tag{7}$$

$$R = H - (z + b) \tag{8}$$

From Fig. 11, for the n-shaped flaw:

$$f_d = \frac{D_o}{2} - (H - R) \tag{9}$$

$$f_d = \frac{D_o}{2} - (z - b) \tag{10}$$

$$R = H - (z - b) \tag{11}$$

The mathematical expression for the width f_w, which is the point of intersection on the x-axis of the circle and horizontal ellipse is determined by considering the following two equations:

$$x^2 + y^2 = r_o^2 \tag{12}$$

$$\frac{x^2}{a^2} + \frac{(y-z)^2}{b^2} = 1 \tag{13}$$

By solving these two equations (as documented fully in Appendix A), the value of f_w in terms of x is obtained from:

$$x = \sqrt{\frac{-B \pm \sqrt{(B^2 - 4AC)}}{2A}} \tag{14}$$

where $A = \left(1 - \frac{b^2}{a^2}\right)^2$; $B = \frac{4b^2z^2}{a^2} + 2\left(1 - \frac{b^2}{a^2}\right)(b^2 + z^2 - r_o^2)$; $C = (b^2 + z^2 - r_o^2)^2 - b^2z^2$

From Eq. (14), f_w of either the n-shaped flawed tube or the u-shaped flawed tube is computed as $2x$ for their full dimension, as shown below:

$$f_w = 2.\sqrt{\frac{-\frac{4b^2z^2}{a^2} + 2\left(1-\frac{b^2}{a^2}\right)(b^2+z^2-r_o^2) \pm \sqrt{\left(\frac{4b^2z^2}{a^2} + 2\left(1-\frac{b^2}{a^2}\right)(b^2+z^2-r_o^2)\right)^2 - 4\left(\left(1-\frac{b^2}{a^2}\right)^2 (b^2+z^2-r_o^2)^2 - 4b^2z^2\right)}}{2\left(1-\frac{b^2}{a^2}\right)^2}} \tag{15}$$

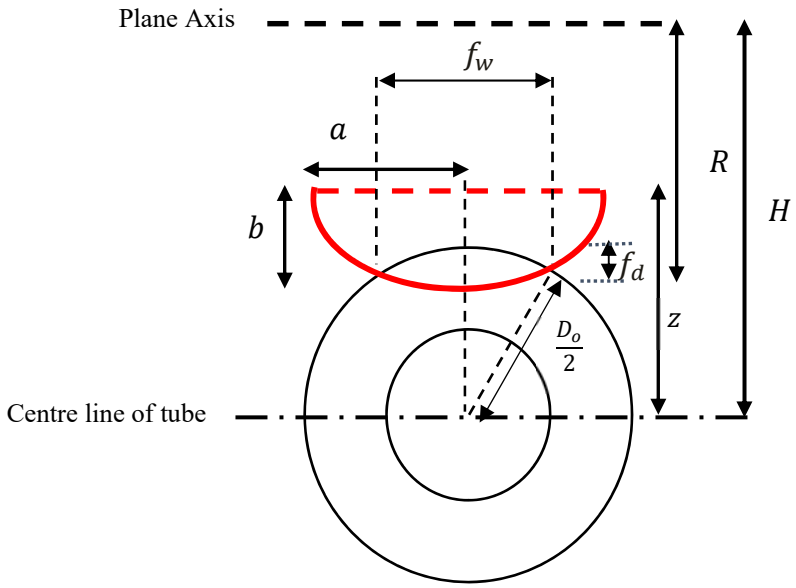

Fig. 10. Front view of the u-shaped flaw showing the cutting plane in red, intersected with the tube cross-section.

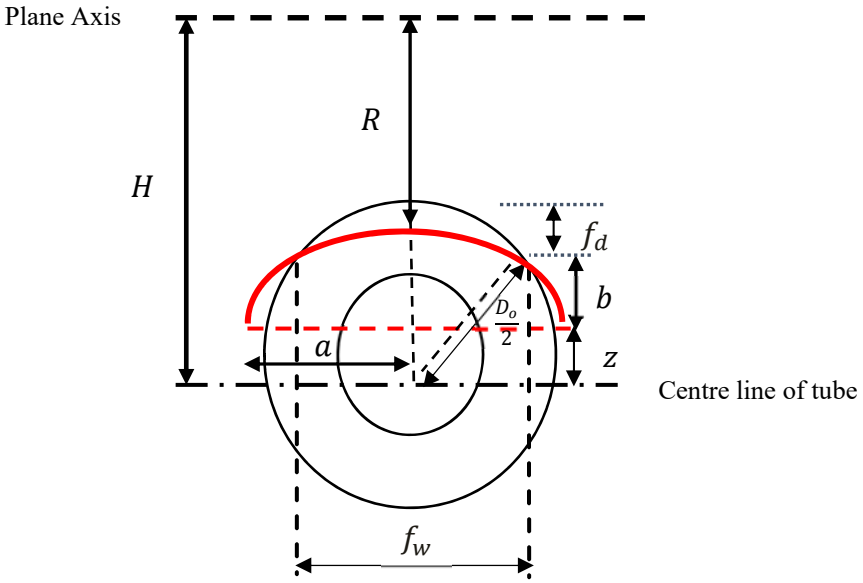

Fig. 11 Front view of the n-shaped flaw showing the cutting plane in red, intersected with the tube cross-section.

The developed mathematical formulations relate the flaw dimensions (f_l, f_w and f_d) of any flawed tube to the geometric model parameters. This is needed for accurate modelling and failure assessment of the tubes, especially for parameterized studies that involve a large number of tubes.

3 Finite element analysis (FEA)

Based on symmetry conditions of the modelled tube, a quarter model is used for the analysis as shown in Fig. 12 (a). This is done to save computation time during the analysis. The entire flawed area is further partitioned to facilitate the easy application of mesh control measures within the main flaw area during the mechanical analysis. Fig. 12 (b) shows the partitioned flawed tube.

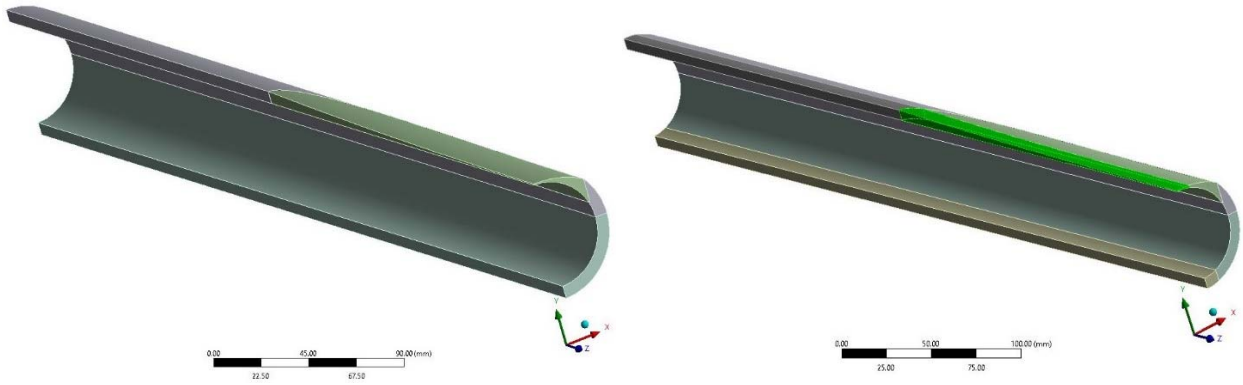

Fig. 12. Quarter n-shaped model showing (a) the entire flaw area and the (b) the partitioned flaw area.

Fourteen flawed tubes with constant flaw length (f_l) and varied flaw width (f_w) for a specific flaw depth (f_d) are modelled. The dimensions and geometric data of the modelled tubes are as follows: D_o = 100 mm, l = 300 mm, t = 10 mm, f_d= 5 mm, H = 500 mm, z = 85 mm (for u-shaped) and z = 5 mm (for n-shaped), b is held constant at 40 mm, while a is varied from 52 mm to 300 mm for the u-shaped, flat line and n-shaped flaw types, as shown in Table 1. The flaw length f_l is kept constant because preliminary studies indicated that the results were insensitive to it [37]. The geometries of the models in relation to their geometry axes and across the length of the tube can be seen in Fig. 13, showing the effect of varying the aspect ratio of the cutting ellipse. When viewed from the cross-section and the side, it can be seen that the flaws modelled have varied widths and fixed constant length and depth. The flat line flaw is shown with a black line in Fig. 13. Notice, in Table 1, that the flaw width for the flat line flaw (TF) is almost identical to that of

the widest u-shaped and n-shaped flaws, TU7 and TN1. For this reason, we do not perform simulations on the flat line flaw.

Material properties are chosen to represent a 15Mo3 low-alloy heat resistant seamless steel boiler tube, with elastic modulus, E = 212 GPa, Poisson's ratio, υ = 0.3, yield strength, σ_y = 260 MPa and ultimate tensile strength, σ_{uts} = 550 MPa. A 20% plastic strain hardening material model ($M_{20\%}$) is used to effectively account for the large percentage plastic strain these tubes experience in reality according to material data sheets [38–42]. Fig. 14 shows this material model, as implemented in ANSYS. In this model, the strain is chosen such that the stress reaches σ_{uts} when the elongation is 20%. After σ_{uts}, the response is perfectly plastic with no further work hardening allowed. The setting of a perfectly plastic response after the elongation limit was done following the guideline stipulated by the American Society of Mechanical Engineers (ASME) in conducting numerical simulation analyses [15]. In this work, the effect of temperature on the material properties is not considered.

Table 1

Geometric dimensions of the modelled tubes

Modelled Tubes	a (mm)	b (mm)	f_l (mm)	f_w (mm)
TU1	52	40	134.54	33.43
TU2	55	40	134.54	34.21
TU3	60	40	134.54	35.34
TU4	70	40	134.54	37.11
TU5	85	40	134.54	38.90
TU6	120	40	134.54	41.06
TU7	300	40	134.54	43.16
TF	N/A	N/A	134.54	43.59
TN1	300	40	134.54	44.03
TN2	120	40	134.54	46.60
TN3	85	40	134.54	50.32
TN4	70	40	134.54	54.88
TN5	60	40	134.54	61.91
TN6	55	40	134.54	69.21
TN7	52	40	134.54	77.08

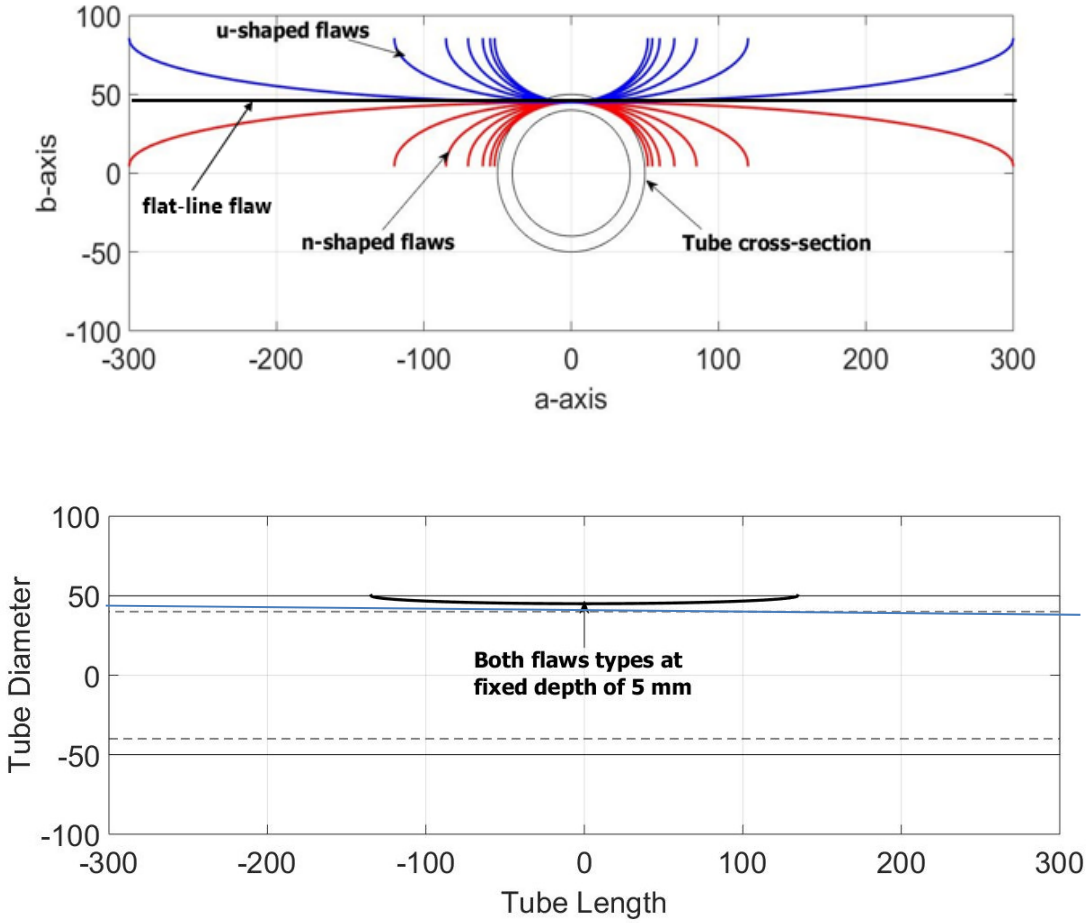

Fig. 13. Cross-sectional view of the geometry plots for the u- and n-shaped flaws at constant flaw length and depth (above); Side view of the geometry plots for both flaws across the tube length (below).

Global meshing of the modelled tubes is performed using mostly hexahedral elements, 2 mm in size. For the flaw area, local mesh control measures are applied to obtain a finer mesh. Body sizing control is used within the flaw area to obtain a finer mesh of 1 mm and soft edge sizing is used to create five sub-divisions along the edge of the remaining thickness (t_r) of the model, as shown in Fig. 15. These measures are taken to ensure each model has good mesh quality and the results that will be obtained from the path created through the tube thickness will be reliable. A mesh convergence check was completed, checking for both element quality and number of elements.

The difference in the hoop stress values between the highest and lowest number of elements was 3.6%.

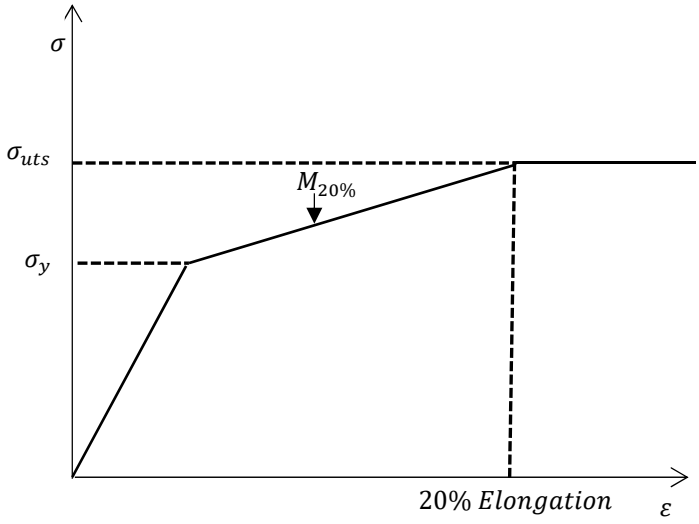

Fig. 14. Material model used for this study

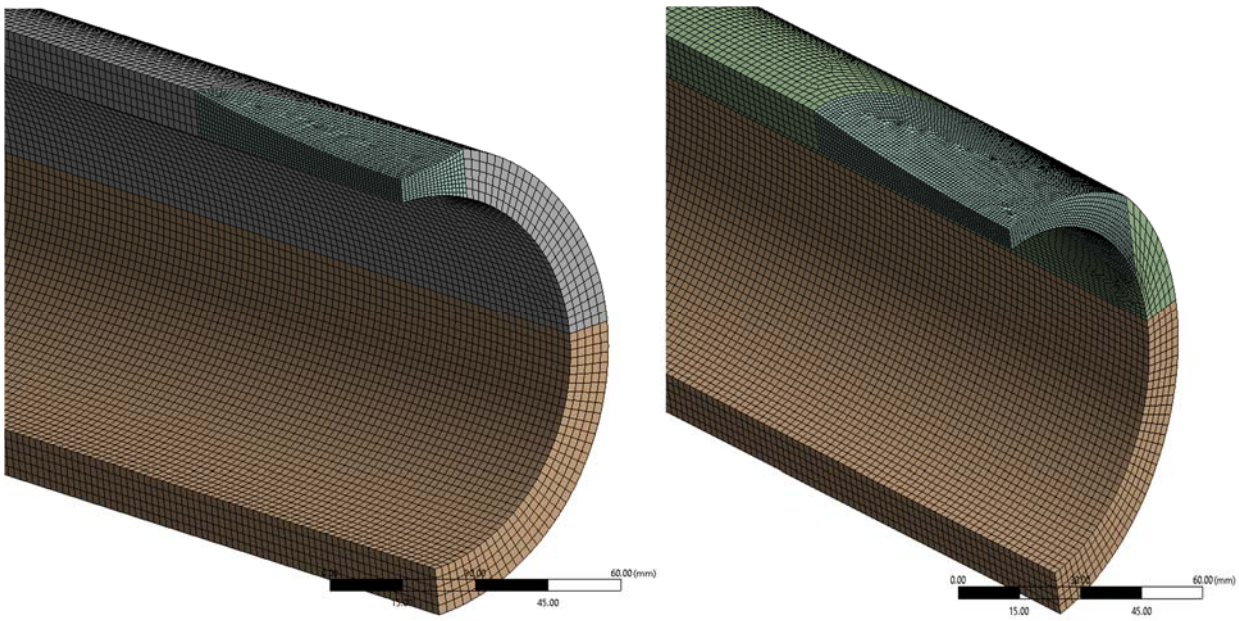

Fig. 15. Samples of meshed u- and n-shaped flawed tubes respectively.

Each modelled tube is solved with a pressure P_a applied on the inner surface of the tube.

$$P_a = \frac{2}{\sqrt{3}} \sigma_{uts} \frac{t_r}{r_i} \tag{16}$$

where t_r and r_i are the tube remaining thickness and inner radius, respectively. This follows directly from the theoretical plastic collapse pressure for flaw-free cylindrical hollow tubes using an elastic-perfect plastic material model [43]. But we replace the yield stress with σ_{uts} (to accommodate the strain hardening of the tube) and the flaw-free thickness, t with t_r (since we were dealing with flawed tubes at a specific tube remaining thickness , t_r). This modified equation enables us to obtain the plastic collapse pressure for these flawed tubes at the deepest point of the flaw, where the Von Mises equivalent stresses are equal to the σ_{uts}. The pressure P_a is therefore used as an estimate of a realistic upper bound for the applied pressure in the finite element model.

Frictionless supports are applied on the symmetrical boundaries of the model and a displacement constraint is applied at the vertex on the lower tip of the model to prevent rigid body motion as shown in Fig. 16. An axial force, $F = P_a\, \pi({D_o}^2/4 - {r_i}^2)$, is applied on the cross-sectional end of the model to introduce the appropriate axial stress without needing to model end cap effects.

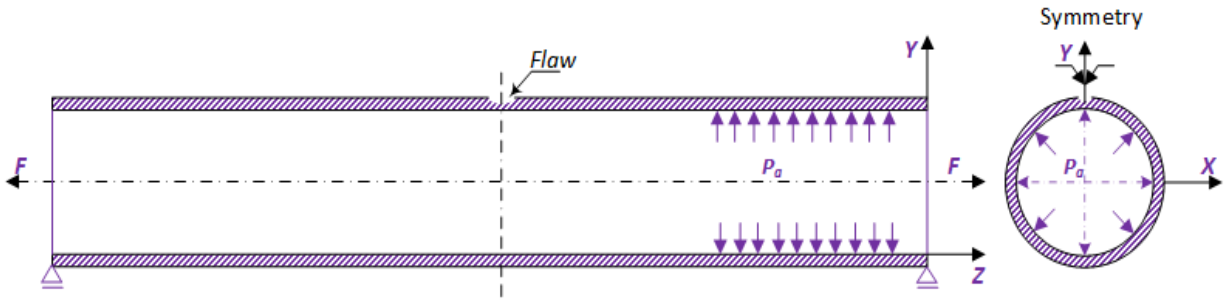

Fig. 16. Load and boundary conditions applied.

4 Results and discussion

4.1 Effect of stress concentration on the failure of the tubes

The elastic stress concentration factors (SCF) of the modelled tubes are computed using:

$$SCF = \frac{\text{Peak Stress}}{\text{Nominal Stress}} \tag{17}$$

where the peak stress is the maximum hoop stress within the localized flaw area of the tube and the nominal stress is given by:

$$\text{Nominal stress} = \frac{Pr_i}{t_r} \tag{18}$$

This represents the stress that would be expected in a uniform tube with thickness t_r.

To calculate the elastic stress concentration factor, the models were solved with loads of $0.1P_a$, ensuring that the tube remained in the elastic domain. Fig. 17 shows the SCF for different flaw geometries of the tubes, which corresponds to different flaw aspect ratios. Note that the u-shaped flaws have a higher SCF within the flawed areas compared to the n-shaped flaws. For both flaw types, as the flaw aspect ratio increases, the SCF within the flaw area decreases. The SCF decreases smoothly with the ratio f_w/f_d for both flaw types, beginning with the smallest u-shaped flaw, U1 (that has the smallest aspect ratio and highest SCF of 1.98) to the largest n-shaped flaw, N7, with the largest aspect ratio and lowest SCF of 1.44. This indicates a 38% variation in SCF using the smallest SCF as reference.

If we consider using the elastic stress analysis to predict failure, then the observed differences in the response of both flaws indicates two outcomes. First, the u-shaped, or scoop, flaws are more susceptible to failing before the n-shaped, or saddle, flaws, and second, the larger the aspect ratios of both flaw types are, the less prone to failure they become. The practical implication of this is

that within similar operating environments, the n-shaped flaws will tend to be less severe compared to the u-shaped ones. Within the family of the u-shaped flaws, the smaller ones are likely to pose more threat compared to the larger ones because of their high SCF.

We will now proceed to investigate the sensitivity of these flaws to the failure pressure of the tubes in the plastic region using nonlinear FEA.

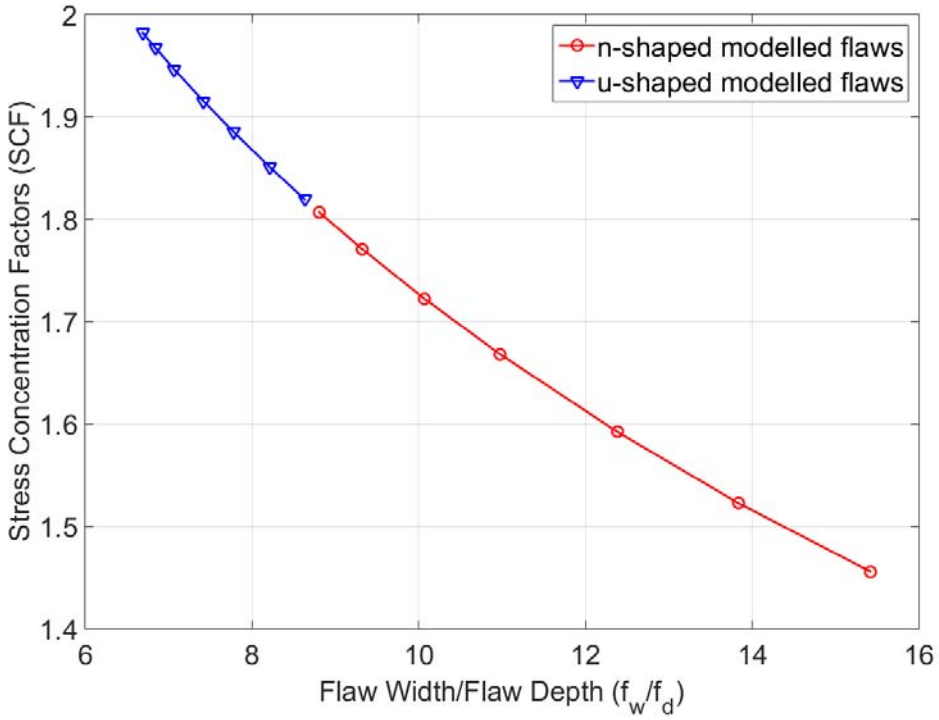

Fig. 17. Stress concentration factors ($SCFs$) for u- and n-shaped flaw width to depth ratios.

4.2 Failure pressure sensitivity to flaw geometry

In this initial investigation on failure pressure, the failure pressure of the tubes is defined as the internal pressure that results in a peak plastic strain of 5%, $P_{5\%}$. Previous research reported on limit load analysis using an elastic perfectly plastic model [3,26,28,32], with some also using 2% plastic strain, $P_{2\%}$ [21,22], as an upper limit. Others used the Von Mises equivalent stress limit σ_{uts} [23–26], without setting a limit on the amount of strain that should be allowed within the

flaw area. Fig. 18 shows the plastic strain distribution of an example of a u-shaped and an n-shaped flaw. It can be seen that the modelled flawed tubes attain 5% plastic strain at the thinnest part of the defect within their flaw area. Notice that the plastic zone is larger for the n-shaped flaw.

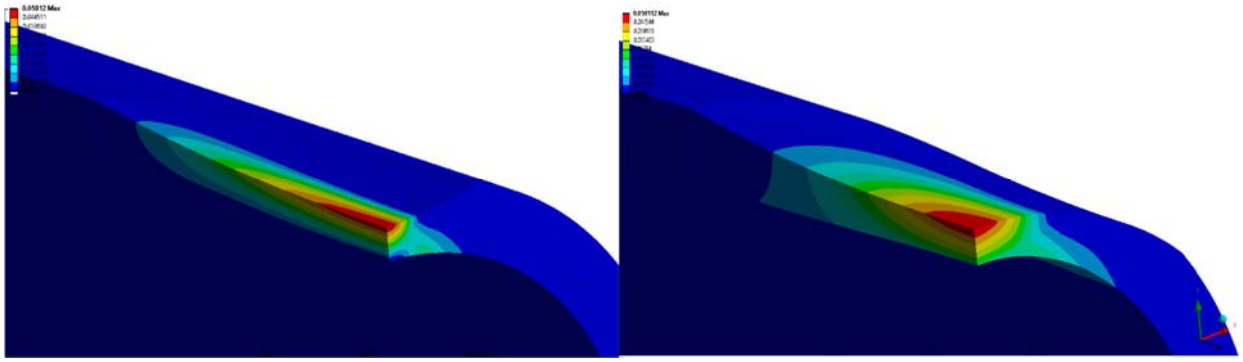

Fig. 18. Plastic strain distribution for the TU1 flaw and TN7 flaw respectively.

Fig. 19 shows the effect of the geometry of the modelled flaws on the failure pressure of the tubes while in plasticity. The failure pressure, $P_{5\%}$, increases from a failure pressure of 50.13 MPa for the u-shaped flaw with the lowest f_w/f_d ratios to 51.36 MPa for the n-shaped flaw with the largest flaw characteristic ratio. It might have been expected that the flaws with small aspect ratios are safer compared to the large aspect ratio flaws, because there is less material removal, but this is not the case. Hence the elastic-plastic analysis results in similar findings to the linear elastic analysis, in that the u-shaped flaws are more severe than the n-shaped ones. However, the failure pressure only varies 2.45% for a flaw width variation from 33.4 mm to 77.1 mm. Therefore, the elastic-plastic analysis shows a reduced sensitivity to shape, only a 2.45% variation compared to 38% variation based on the linear elastic analysis.

From the outcome of the previous assessment and this one, it can be inferred that, as a result of the stress redistribution that occurs after yielding, the flaw geometry only slightly influences the failure of the tube. Note that we have not altered the flaw depth. The failure pressure based on linear elasticity is inversely proportional to minimum remaining wall thickness, and extensive

nonlinear finite element analyses on similar geometries indicate that tube failure is highly sensitive to minimum remaining wall thickness [35,44].

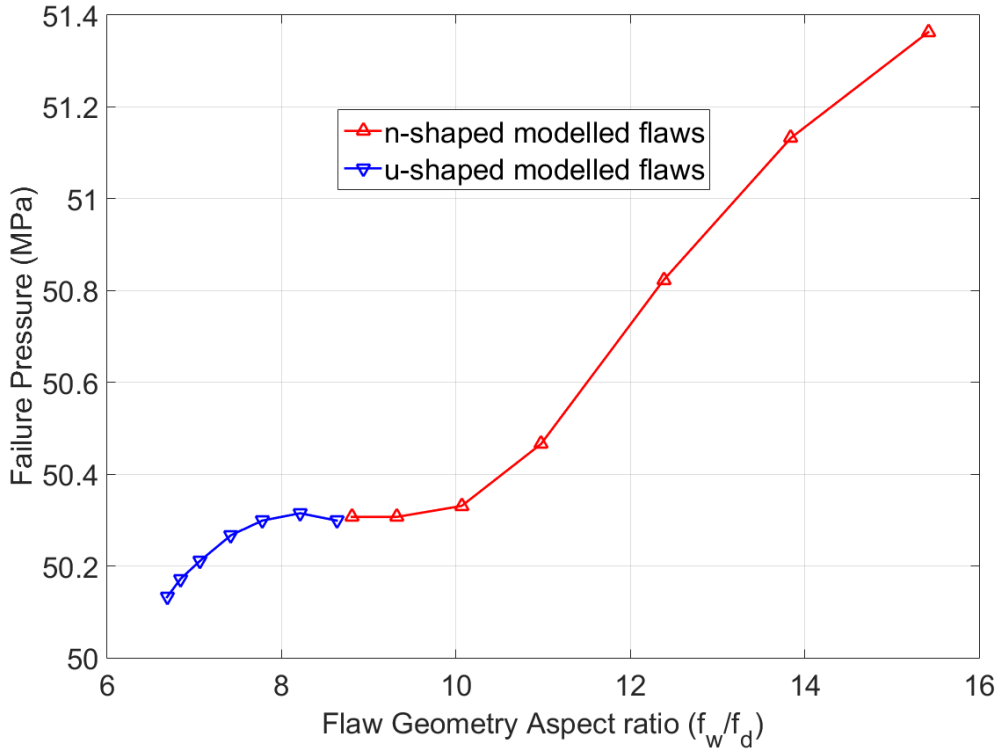

Fig. 19. Failure pressure for different flaw geometries of the modelled tubes

4.3 Sensitivity of various failure criteria on flaw geometry

Failure pressures of the modelled tubes are analysed again, but now based on a broad range of failure criteria from literature, as reported in the introduction. These criteria include: 2% plastic strain ($P_{2\%}$) [21,22], 0.9. σ_{uts} [27,28] and 0.8 σ_{uts} [28]. Additional criteria are also investigated, which include: 20% plastic strain ($P_{20\%}$), 15% plastic strain ($P_{15\%}$), 10% plastic strain ($P_{10\%}$), 7.5% plastic strain ($P_{7.5\%}$) and 5% plastic strain ($P_{5\%}$) criteria. This deliberately broad range of criteria aims to ensure that our conclusions are general, and not specific for one single criterion.

The large strain hardening model selected ($M_{20\%}$) allowed the analyses to proceed to 20% plastic strain, $P_{20\%}$. We acknowledge that this is an unreasonable upper bound for a practical failure

criterion, but we want to observe the behaviour of the flaws up to this numerical upper limit. Beyond $P_{20\%}$, the material model is perfectly plastic, and then plastic strain localization occurs and the models no longer converge. The peak failure pressures based on each failure criterion are obtained from each of the modelled tubes. Fig. 20 shows the effect of the flaw geometry on the failure of the tubes based on the criterion used. It can be first noticed that for all the failure criteria, except the lowest one ($P_{2\%}$), they follow the same pattern as had been reported from the outcome of the previous investigations done [37,45], with the n-shaped flaws generally having higher failure pressure compared the u-shaped ones. However, the differences are small. Table 2 summarizes the smallest and largest failure pressures, for each of the considered failure criteria. The differences are less than 10% for all the failure criteria, with the $P_{20\%}$ case having the highest difference of 9.13%.

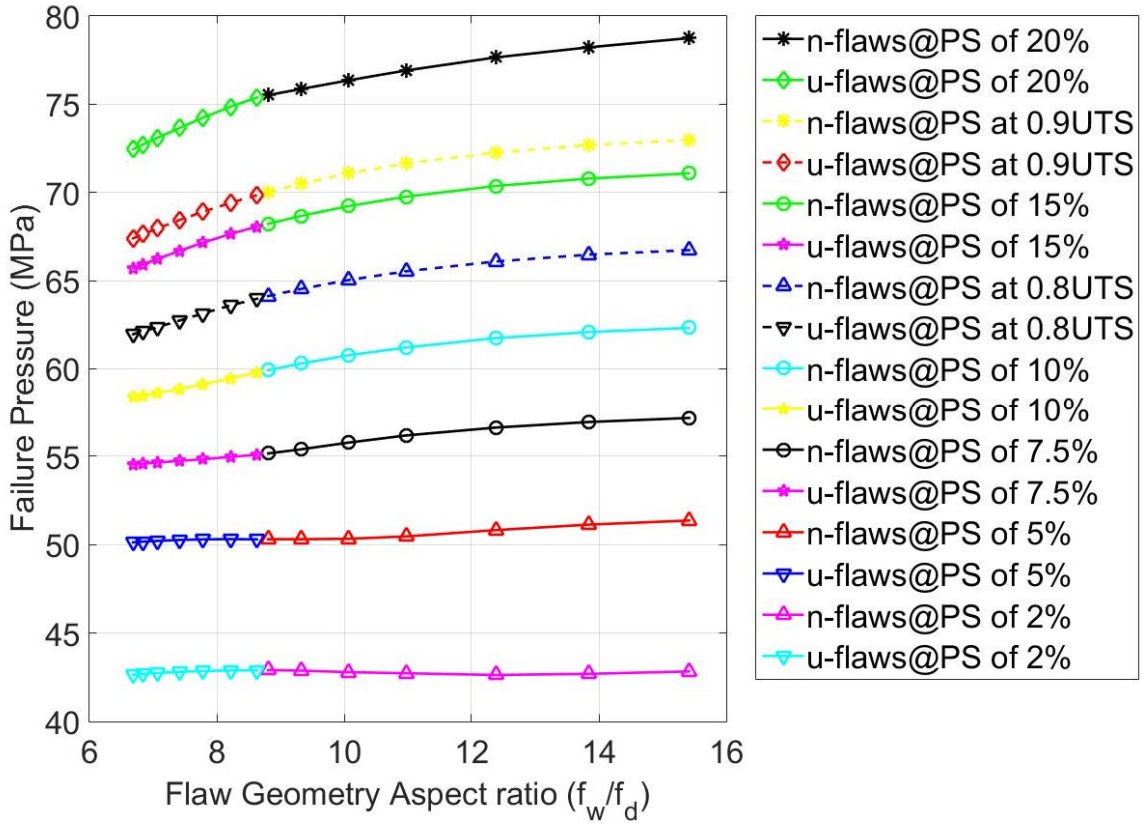

Fig. 20. Failure pressure for different flaw geometry of modelled tubes based on various failure criteria.

Table 2

Percentage differences between the failure pressure of the largest and smallest flaws for each failure criteria.

Failure Criteria	Maximum Failure Pressure (MPa)	Minimum Failure Pressure (MPa)	Percentage Difference (%)
$P_{20\%}$	78.88	72.28	9.13
$0.9.\sigma_{uts}$	73.06	67.21	8.70
$P_{15\%}$	71.62	66.02	8.48
$0.8.\sigma_{uts}$	67.08	62.22	7.81
$P_{10\%}$	62.26	58.15	7.07
$P_{7.5\%}$	57.18	54.92	4.12
$P_{5\%}$	51.36	50.13	2.45
$P_{2\%}$	42.71	42.62	0.21

This investigation made it clear that the failure of externally eroded tubes is only slightly sensitive to the flaw width, even for variation across a large range (flaw width from 33.4 mm to 77.1 mm). In previous works, we have shown that the sensitivity to flaw length is equally small [37], but the sensitivity to minimum remaining wall thickness is high [35]. Therefore, we conclude that failure assessment of externally eroded tubes can be performed reasonably well without requiring precise measurements of flaw width and flaw length. It is also a reasonable extrapolation from these results to conclude that the failure assessments would be similarly insensitive to a different shape assumption, as long as the same minimum remaining wall thickness is used.

5 Conclusions

In this paper, using a distinctive procedure, three variants of geometric flaw shapes that reasonably satisfy a wide range of real localized erosion flaw geometries were modelled. Geometric functions that could accurately model real localized thinned tubes were formulated from the developed models. These geometric functions find much relevance in conducting parameterized studies and failure assessment for cases involving a large number of tubes.

Linear finite element analysis was first carried out on the modelled tubes to examine the effect of stress concentration on the failure of the tubes due to localized external erosion. It was observed

that the u-shaped flaws were more susceptible to elastic stress concentration than the n-shaped flaws, and also, the larger the aspect ratios of both flaw types, the lower the elastic stress concentration factor. The practical implication of this is that within a similar operating environment, the n-shaped flaws will tend to be less severe than the u-shaped ones.

Following this assessment, failure pressures of the tubes were predicted using nonlinear finite element analyses on the modelled flaw geometries based on the internal pressure that results in a peak plastic strain of 5%, $P_{5\%}$. The outcome of this investigation shows that the failure pressure increases proportionately from a low failure pressure for the u-shaped flaw with the lowest f_w/f_d ratios to a slightly higher failure pressure for the n-shaped flaw with the largest flaw characteristic ratio. The implication of this is that n-shaped flaws will be able to withstand more pressure as they deform plastically for the same percentage elongation when compared to their u-shaped counterparts. This finding reinforces the earlier result on the effect of elastic stress concentration that the u-shaped flaws were more severe than the n-shaped ones.

However, the increase in failure pressure as flaw shape changes is small (2.45%). Therefore, the most important research finding in this paper is that the failure assessment of externally eroded boiler tubes is insensitive to the specific shape parameterization employed, as long as the minimum remaining wall thickness is matched. Any reasonable shape that matches the flaw width, flaw length and minimum remaining wall thickness will produce failure pressure predictions that only differ marginally.

Finally, failure pressures of the modelled tubes were computed based on other failure criteria obtained from literature and some suggested by the authors. This study showed that the prior conclusion holds for all reasonable failure criteria: the failure assessment of boiler tube flaws is insensitive to the specific choice of shape parameterization.

Overall, the insights gained from this study suggests a specific future avenue for failure assessment of boiler tubes. Since the specific form of the shape parameterization is not absolutely critical, numerous finite element models can be generated using a simple parameterization. These large number of models can then be analyzed off-line, potentially producing a database of known results that can be used for rapid decision making once a specific flaw is identified.

Acknowledgements

The authors are grateful to the University of Pretoria Doctoral Commonwealth Scholarship and the Centre for Asset Integrity Management at the University of Pretoria for the financial support and assistance rendered for this study.

References

[1] P. Haribhakti, P.B. Joshi, R. Kumar, Failure Investigation of Boiler Tubes: A Comprehensive Approach, ASM International, 2018.
[2] K. Zarrabi, Estimation of boiler tube life in presence of corrosion and erosion processes, International Journal of Pressure Vessels & Piping. 53 (1993) 351–358.
[3] K. Zarrabi, H. Zhang, Creep and plastic collapse lives of scarred boiler tubes, Materials at High Temperatures. 15 (1998) 389–393.
[4] D.N. French, Metallurgical failures in fossil fired boilers, John Wiley and Sons, Inc. (1993).
[5] A.K. Pramanick, G. Das, S.K. Das, M. Ghosh, Failure investigation of super heater tubes of coal fired power plant, Case Studies in Engineering Failure Analysis. 9 (2017) 17–26.
[6] ASM Handbook Committee, Failure Analysis and Prevention, 2002.
[7] B. Dooley, P.S. Chang, The current state of boiler tube failures in fossil plants, PowerPlant Chemistry. 2 (2000) 197–203.
[8] J.F. Drennen, P. Kratina, Guidelines for control and prevention of fly ash erosion in fossil fired power plants. Final report by EPRI, USA., 1994.
[9] J. Roy-Aikins, Challenges in meeting the electricity needs of South Africa, in: Proceedings of the ASME 2016 Power and Energy Conference (PowerEnergy2016-59085), 2016: p. V001T05A002.
[10] G.P. Sullivan, R. Pugh, A.P. Melendez, W.D. Hunt, Operations and maintenance best practices: A guide to achieving operational efficiency, 2010.
[11] K. Zarrabi, A comparison of several boiler tube life prediction methods, International Journal of Pressure Vessels & Piping Vessels & Piping. 58 (1994) 197–201.
[12] M. Suckling, C. Allen, Critical variables in high temperature erosive wear, Wear. 203–204 (1997) 528–536.
[13] Electric Power Research Institute (EPRI), Guidelines for control and prevention of fly ash

erosion, 2011.
[14] S.W. Liu, W.Z. Wang, C.J. Liu, Failure analysis of the boiler water-wall tube, Case Studies in Engineering Failure Analysis. 9 (2017) 35–39.
[15] American Society of Mechanical Engineers (ASME), ASME Boiler and Pressure Vessel Code, Division 2, Section VIII Rules for Construction of Pressure Vessels, 2015.
[16] M. Muscat, D. Mackenzie, R. Hamilton, A work criterion for plastic collapse, International Journal of Pressure Vessels and Piping. 80 (2003) 49–58.
[17] J. Ahmad, J. Purbolaksono, L.C. Beng, A.Z. Rashid, A. Khinani, A.A. Ali, Failure investigation on rear water wall tube of boiler, Engineering Failure Analysis. 16 (2009) 2325–2332.
[18] Y. Gong, Z. Yang, J. Yuan, Failure analysis of leakage on titanium tubes within heat exchangers in a nuclear power plant. Part II : Mechanical degradation, Materials and Corrosion. 63 (2012) 18–28.
[19] F.-J. Chen, C. Yao, Z. Yang, Failure analysis on abnormal wall thinning of heat-transfer titanium tubes of condensers in nuclear power plant Part II: Erosion and cavitation corrosion, Engineering Failure Analysis. 37 (2014) 42–52.
[20] H. Wang, Y. Yu, J. Yu, W. Xu, X. Li, S. Yu, Numerical simulation of the erosion of pipe bends considering fluid-induced stress and surface scar evolution, Wear. 440–441 (2019) 203043. doi:10.1016/j.wear.2019.203043.
[21] J.R. Sims, B.F. Hantz, K.E. Kuehn, A basis for the fitness for service evaluation, Pressure Vessel Fracture, Fatigue, and Life Managment, ASME PVP. 233 (1992) 51–58.
[22] B.F. Hantz, J.R. Sims, C.T. Kenyon, T.A. Turbak, Fitness for service: Groove-like local thin-areas on pressure vessels and storage tanks, Plant Systems/Components Aging Management, ASME PVP. 252 (1993).
[23] D.-J. Shim, J. Choi, Y. Kim, Failure strength assessment of pipes with local wall thinning under combined loading based on finite element analyses, Journal of Pressure Vesssel Technology. 126 (2004) 179–183.
[24] D.-J. Shim, Y.-J. Kim, Y.-J. Kim, Reference stress based approach to predict failure strength of pipes with local wall thinning under combined loading, Journal of Pressure Vessel Technology. 127 (2005) 76. doi:10.1115/1.1849228.
[25] G. Fekete, L. Varga, The effect of the width to length ratios of corrosion defects on the burst pressures of transmission pipelines, Engineering Failure Analysis. 21 (2012) 21–30.
[26] J.E. Abdalla Filho, R.D. Machado, R.J. Bertin, M.D. Valentini, On the failure pressure of pipelines containing wall reduction and isolated pit corrosion defects, Computers and Structures. 132 (2014) 22–33.
[27] Y. Kim, Y. Lee, W. Kim, K. Oh, The evaluation of failure pressure for corrosion defects within girth or seam weld in transmission pipelines, in: Proceedings of the Intenational Pipeline Conference (IPC2004-216), 2004: pp. 1–9.
[28] J.B. Choi, B.K. Goo, J.C. Kim, Y.J. Kim, W.S. Kim, Development of limit load solutions for corroded gas pipelines, International Journal of Pressure Vessels and Piping. 80 (2003) 121–128.
[29] J.W. Kim, C.Y. Park, S.H. Lee, Local failure criteria for wall-thinning defect in piping components based on simulated specimen and real-scale pipe tests, in: 20th International Conference on Structural Mechanics in Reactor Technology (SMiRT 20), 2009: pp. 1–14.
[30] B. Ma, J. Shuai, D. Liu, K. Xu, Assessment on failure pressure of high strength pipeline with corrosion defects, Engineering Failure Analysis. 32 (2013) 209–219.

[31] M. Kamaya, T. Suzuki, T. Meshii, Failure pressure of straight pipe with wall thinning under internal pressure, International Journal of Pressure Vessels and Piping. 85 (2008) 628–634. doi:10.1016/j.ijpvp.2007.11.005.
[32] K. Zarrabi, H. Zhang, Primary stress in scarred boiler tubes, International Journal of Pressure Vessels and Piping. 65 (1996) 157–161.
[33] K. Zarrabi, Plastic collapse pressures for defected cylindrical vessels, International Journal of Pressure Vessels & Piping. 60 (1994) 65–69.
[34] D.R. Stephens, B.N. Leis, Material and geometry factors controlling failure of corrosion defects in piping, in: International Pressure Vessels and Piping Conference, 1997.
[35] I.E. Kalu, H.M. Inglis, S. Kok, Failure assessment methodology for boiler tubes with localized erosion defects, International Journal of Pressure Vessels & Piping. (2020). doi:https://doi.org/10.1016/j.ijpvp.2020.104190.
[36] ANSYS® 2019 R2 Academic Research Version, (2019).
[37] I.E. Kalu, H.M. Inglis, S. Kok, Effect of defect geometry of localized external erosion on failure of boiler tubes, in: Proceedings of the ASME 2018 Pressure Vessels and Piping Conference, Volume 3B: Design and Analysis, Prague, Czech Republic, 2018: p. V03BT03A037. doi:https://doi.org/10.1115/PVP2018-84787.
[38] American Society of Mechanical Engineers (ASME), ASME Boiler and Pressure Vessel Code, Section II, Part D: Materials Properties, 2015.
[39] Deutsche Normen, DIN-17175 Seamless tubes of heat-resistant steels, 1979.
[40] British Standards Institution (BSI), BS-EN-10216-Seamless steel tube for pressure purposes - Part 2, 2002.
[41] D. Gandy, Carbon steel handbook, Electric Power Research Institute (EPRI), 2007.
[42] J.E. Bringas, Handbook of comparative world steel standards, 3rd Ed., ASTM, 2002.
[43] H. Koboyashi, T. Ogawa, Evaluation of corroded and artificially flawed vessels, in: High Presssure Technology at the Dawn of the New Millenium ASME PVP-Vol. 418, 2001: pp. 69–75.
[44] I.E. Kalu, Failure assessment of boiler tubes under localized external erosion to support maintenance decision, Ph.D. Thesis, University of Pretoria, 2020.
[45] I.E. Kalu, H.M. Inglis, S. Kok, Non-linear finite element analysis of boiler tubes under localized thinning caused by wall loss mechanisms, in: Proceedings of the 11th South African Conference on Computational and Applied Mechanics (SACAM), 2018: pp. 280–290.

Appendix A

To formulate the mathematical expression for the flaw width, f_w, the point of intersection on the x-axis of the circle and ellipse need to be determined, the two simultaneous equations below are considered:

For the circle:

$$x^2 + y^2 = r_o^2 \quad \text{(A 1)}$$

For the ellipse:

$$\frac{x^2}{a^2} + \frac{(y-z)^2}{b^2} = 1 \quad \text{(A 2)}$$

From A 2,

$$b^2x^2 + a^2(y-z)^2 = a^2b^2 \quad \text{(A 3)}$$

$$a^2(y-z)^2 = a^2b^2 - b^2x^2 \quad \text{(A 4)}$$

$$(y-z)^2 = \frac{b^2(a^2-x^2)}{a^2} \quad \text{(A 5)}$$

$$\mathrm{y} = \frac{\mathrm{b}\sqrt{(\mathrm{a}^2-\mathrm{x}^2)}}{\mathrm{a}} + \mathrm{z} \quad \text{(A 6)}$$

Substituting A 6 into A 1;

$$x^2 + \left(\frac{b\sqrt{(a^2-x^2)}}{a} + z\right)^2 = r_o^2 \quad \text{(A 7)}$$

$$x^2 + \frac{b^2}{a^2}(a^2-x^2) + z^2 + \frac{2bz}{a}\sqrt{(a^2-x^2)} = r_o^2 \quad \text{(A 8)}$$

$$\left(1 - \frac{b^2}{a^2}\right)x^2 + b^2 + z^2 + \frac{2bz}{a}\sqrt{(a^2-x^2)} = r_o^2 \quad \text{(A 9)}$$

$$\left(1 - \frac{b^2}{a^2}\right)x^2 + b^2 + z^2 - r_o^2 = -\frac{2bz}{a}\sqrt{(a^2-x^2)} \quad \text{(A 10)}$$

$$\left(\left(1 - \frac{b^2}{a^2}\right)x^2 + b^2 + z^2 - r_o^2\right)^2 = \left(-\frac{2bz}{a}\sqrt{(a^2-x^2)}\right)^2 \quad \text{(A 11)}$$

$$\left(1-\frac{b^2}{a^2}\right)^2 x^4 + (b^2+z^2-r_o^2)^2 + 2\left(1-\frac{b^2}{a^2}\right)x^2(b^2+z^2-r_o^2) = \frac{4b^2z^2}{a^2}(a^2-x^2) \qquad \text{(A 12)}$$

$$\left(1-\frac{b^2}{a^2}\right)^2 x^4 + \left[\frac{4b^2z^2}{a^2} + 2\left(1-\frac{b^2}{a^2}\right)(b^2+z^2-r_o^2)\right]x^2 + [(b^2+z^2-r_o^2)^2 - 4b^2z^2] = 0 \qquad \text{(A 13)}$$

Let $t = x^2$,

$$At^2 + Bt + C = 0 \qquad \text{(A 14)}$$

$$t = \frac{-B \pm \sqrt{(B^2-4AC)}}{2A} \qquad \text{(A 15)}$$

$$x = \sqrt{\frac{-B \pm \sqrt{(B^2-4AC)}}{2A}} \qquad \text{(A 16)}$$

$$where\ A = \left(1-\frac{b^2}{a^2}\right)^2;\ B = \frac{4b^2z^2}{a^2} + 2\left(1-\frac{b^2}{a^2}\right)(b^2+z^2-r_o^2);\ C = (b^2+z^2-r_o^2)^2 - b^2z^2$$

Since $f_w = 2x$, then,

$$f_w = 2.\sqrt{\frac{-\frac{4b^2z^2}{a^2}+2\left(1-\frac{b^2}{a^2}\right)(b^2+z^2-r_o^2) \pm \sqrt{\left(\left(\frac{4b^2z^2}{a^2}+2\left(1-\frac{b^2}{a^2}\right)(b^2+z^2-r_o^2)\right)^2 - 4\left(\left(1-\frac{b^2}{a^2}\right)^2(b^2+z^2-r_o^2)^2 - 4b^2z^2\right)\right)}}{2\left(1-\frac{b^2}{a^2}\right)^2}}$$